A&A 673, A39 (2023)
https://doi.org/10.1051/0004-6361/202244694

Astronomy & Astrophysics

Morphology of the gas-rich debris disk around HD 121617 with SPHERE observations in polarized light⋆

Clément Perrot[1,2,3], Johan Olofsson[4,2,3], Quentin Kral[1], Philippe Thébault[1], Matías Montesinos[5,3], Grant Kennedy[6,7], Amelia Bayo[8,2,3], Daniela Iglesias[9], Rob van Holstein[10], and Christophe Pinte[11,12]

[1] LESIA, Observatoire de Paris, Université PSL, CNRS, Sorbonne Université, Université Paris Cité, 5 place Jules Janssen, 92195 Meudon, France
e-mail: clement.perrot@obspm.fr
[2] Instituto de Física y Astronomía, Facultad de Ciencias, Universidad de Valparaíso, Av. Gran Bretaña 1111, Valparaíso, Chile
[3] Núcleo Milenio Formación Planetaria – NPF, Universidad de Valparaíso, Av. Gran Bretaña 1111, Valparaíso, Chile
[4] Max Planck Institute for Astronomy, Königstuhl 17, 69117 Heidelberg, Germany
[5] Escuela de Ciencias, Universidad Viña del Mar, Viña del Mar, Chile
[6] Department of Physics, University of Warwick, Gibbet Hill Road, Coventry CV4 7AL, UK
[7] Centre for Exoplanets and Habitability, University of Warwick, Gibbet Hill Road, Coventry CV4 7AL, UK
[8] European Southern Observatory, Karl-Schwarzschild-Strasse 2, 85748 Garching bei München, Germany
[9] School of Physics and Astronomy, Sir William Henry Bragg Building, University of Leeds, Leeds LS2 9JT, UK
[10] European Southern Observatory, Alonso de Cordova 3107, Vitacura, Casilla 19001, Santiago 8320000, Chile
[11] School of Physics and Astronomy, Monash University, Vic 3800, Australia
[12] Univ. Grenoble Alpes, CNRS, IPAG, 38000 Grenoble, France

Received 5 August 2022 / Accepted 6 February 2023

ABSTRACT

Context. Debris disks are the signposts of collisionally eroding planetesimal circumstellar belts, whose study can put important constraints on the structure of extrasolar planetary systems. The best constraints on the morphology of such disks are often obtained from spatially resolved observations in scattered light. In this paper, we investigate the young (∼16 Myr) bright gas-rich debris disk around HD 121617.

Aims. We use new scattered light observations from VLT/SPHERE to characterize the morphology and the dust properties of the debris disk. From these properties, we can then derive constraints on the physical and dynamical environment of this system, for which significant amounts of gas have been detected.

Methods. The disk morphology is constrained by linear polarimetric observations in the *J* band. Based on our modeling results and archival photometry, we also model the spectral energy distribution (SED) to put constraints on the total dust mass and dust size distribution. Finally, we explore different scenarios that could explain these new constraints.

Results. We present the first resolved image in scattered light of the debris disk around HD 121617. We fit the morphology of the disk, finding a semi-major axis of 78.3 ± 0.2 au, an inclination of 43.1 ± 0.2°, and a position angle of the major axis with respect to north of 239.8 ± 0.3°, which is compatible with the previous continuum and CO detection with ALMA. Our analysis shows that the disk has a very sharp inner edge, possibly sculpted by a yet-undetected planet or gas drag. While less sharp, its outer edge is steeper than expected for an unperturbed disk, which could also be due to a planet or gas drag, but future observations probing the system farther from the main belt would help explore this possibility further. The SED analysis leads to a dust mass of 0.21 ± 0.02 $M_\oplus$ and a minimum grain size of 0.87 ± 0.12 µm, smaller than the blowout size by radiation pressure, which is not unexpected for very bright collisionally active disks.

Key words. techniques: polarimetric – techniques: high angular resolution – methods: observational – infrared: planetary systems – protoplanetary disks – zodiacal dust

1. Introduction

Debris disks are circumstellar disks orbiting around stars older than 10 Myr. They are detected around stars of all types and of all ages (e.g., Wyatt et al. 2007; Sibthorpe et al. 2018), and they are found around up to 75% of the stars in the youngest moving groups (e.g., the F stars in the β Pic moving group, Pawellek et al. 2021). Debris disks are observed via ≤1 mm dust produced by destructive collisions between solid bodies up to 1–100s of km in size (Krivov & Wyatt 2021). Most of the mass of a debris disk is contained in the largest of these solid bodies that constitute planetesimal belts similar to the Kuiper belt objects (KBOs) in our Solar System. Though these large bodies cannot be observed in extrasolar systems, the location of the planetesimal belts can be probed in the millimeter, which targets the thermal emission of large millimeter-sized grains that are unaffected by stellar radiation pressure and thus have a dynamic similar to their larger parent bodies (e.g., Matrà et al. 2019). In contrast, scattered light observations (e.g., at near-infrared wavelengths with SPHERE, Perrot et al. 2019) probe much smaller micron-sized dust, whose orbits are strongly affected by radiation pressure and whose locations might strongly depart from that of the planetesimal belt (Thébault et al. 2014).

⋆ Reduced images are only available at the CDS via anonymous ftp to cdsarc.cds.unistra.fr (130.79.128.5) or via https://cdsarc.cds.unistra.fr/viz-bin/cat/J/A+A/673/A39

Detecting and spatially resolving debris disks in scattered light using extreme adaptive optics high-contrast imagers (e.g., SPHERE, GPI, SCExAO; Beuzit et al. 2019; Macintosh et al. 2014; Jovanovic et al. 2015) or space telescopes (e.g., HST Ford et al. 2003) has now become common (e.g., Esposito et al. 2020; Schneider et al. 2014; Feldt et al. 2017; Lagrange et al. 2016; Perrot et al. 2016). Linearly polarized light can also be observed with the Very Large Telescope/Spectro Polarimetric High contrast Exoplanet REsearch (VLT/SPHERE) instrument, which provides an alternative and sensitive method to detect debris disks surrounding bright stars emitting unpolarized light (e.g., Engler et al. 2017; Olofsson et al. 2016; Arriaga et al. 2020, among others.). These polarimetric observations reach a contrast close to the photon-noise limit (van Holstein et al. 2021, Appendix E), and the extracted disk parameters do not suffer from self-subtraction effects (Milli et al. 2012), as are seen with angular differential imaging (ADI; Marois et al. 2006) in total intensity. Polarized light provides additional information on the optical properties of dust compared to the total intensity signal (e.g., Milli et al. 2019; Singh et al. 2021; Crotts et al. 2021). Thanks to the very high contrast and spatial resolution of SPHERE, remarkably sharp and deep images of debris disks can be obtained (e.g., Boccaletti et al. 2018; Olofsson et al. 2018), which provide information on the spatial distribution of dust that can be used to derive important information about the global structure of the planetary system (e.g., Lee & Chiang 2016). As an example, the detection of a sharp inner edge of a disk could be interpreted as the signature of a planet located close to the disk's edge and that has cleared all dust from its chaotic zone (e.g., Wisdom 1980; Quillen & Faber 2006; Lagrange et al. 2012).

Another potential mechanism that could shape the radial structure of a debris ring, with possible consequences on its inner and outer edges, is the drag due to gas, as it will selectively make small dust grains drift inward or outward, depending on their sizes (Takeuchi & Artymowicz 2001; Olofsson et al. 2022). These considerations are important because gas is now being detected in debris disks (e.g., Zuckerman & Song 2012; Hughes et al. 2018). In fact, mainly thanks to the Atacama Large Millimeter and Submillimeter Array (ALMA), the presence of gas in a young bright debris disk has been shown to be the norm rather than the exception (Moór et al. 2017). The observed gas (mainly CO, carbon, and oxygen) is thought to be released from volatiles contained initially in icy form in the planetesimals of these debris disk belts, providing access to the composition of the volatile phase of the KBO-like bodies (e.g., Zuckerman & Song 2012; Kral et al. 2016). In this scenario, both dust and gas would be of secondary origin. However, for the most massive gas disks, and only those, it is still possible that the observed gas is a relic of the protoplanetary disk phase that takes longer than expected to dissipate (e.g., Kóspál et al. 2013; Nakatani et al. 2021). Such a primordial origin is, however, not necessary because the presence of large amounts of CO can also be explained by the gas released from planetesimals, which creates a layer of neutral carbon gas and shields CO from photodissociation (Kral et al. 2019).Some observational evidence seems to make the primordial origin less convincing than the secondary hypothesis (Hughes et al. 2017; Smirnov-Pinchukov et al. 2022). In systems with a significant amount of gas, interactions between gas and dust may become important and affect the dust size distribution at the smallest sizes, which may leave observable imprints (e.g., Bhowmik et al. 2019; Moór et al. 2019; Olofsson et al. 2022).

In this paper, we study the debris disk around the young A1V star HD 121617, which is also surrounded by a massive gas disk (Moór et al. 2017). More precisely, our new study presents the first resolved scattered light observations of the debris disk around HD 121617 obtained at the J band in polarization with SPHERE. This debris disk has been known for about 25 yr, and it has now been observed at a range of wavelengths, from optical to millimeter (Mannings & Barlow 1998; Cutri et al. 2012; Moór et al. 2017). Its fractional luminosity is close to 5×10^{-3} (Moór et al. 2011), which places it among the brightest disks observed to date. More information on the star and its disk is provided in Sect. 2. In Sect. 3, we present the new SPHERE observations of HD 121617. In Sect. 4, we present the morphological analysis of the disk based on our resolved observations. In Sect. 5, we present the spectral energy distribution (SED) analysis of the system, which allows us to recover information on the dust size distribution and total dust mass. Finally, in Sect. 6, we discuss our results before concluding in Sect. 7.

2. HD 121617

2.1. Stellar parameters

The star HD 121617 is an A1V (Houk 1978) main sequence star (Matrà et al. 2018), is member of the Upper Centaurus Lupus (UCL) association (Hoogerwerf 2000; Gagné et al. 2018), and has an estimated age of 16 ± 2 Myr, based on the age of the UCL association (Pecaut & Mamajek 2016). The distance of the star is 117.9 ± 0.5 pc (DR3, Gaia Collaboration 2016, 2023). The most recent estimations of the stellar parameters are reported in different studies, for example, in Rebollido et al. (2018), where the authors estimated the effective temperature to be $T_{\rm eff} = 9285$ K and the surface gravity of $\log g = 4.45$. In Cotten & Song (2016), the effective temperature is estimated at $T_{\rm eff} = 8710$ K and a stellar radius at $R_\star = 1.63\,R_\odot$, while Matrà et al. (2018) estimated the stellar luminosity at $L_\star = 17.3\,L_\odot$ and the stellar mass at $M_\star = 1.9\,M_\odot$. The galactic extinction estimated by *Gaia* DR3 is to $A_0 = 0.1331^{+0.0012}_{-0.0018}$ mag (Gaia Collaboration 2016, 2023) and the ratio between the extinction and the reddening to $R_V = 3.25$ (Gontcharov & Mosenkov 2018).

2.2. Debris disk in the infrared

The presence of a disk around HD 121617 was first reported in Mannings & Barlow (1998) as an infrared excess at 12, 25, 60, and 100 µm in the Infrared Astronomical Satellite (IRAS) Faint Source Survey Catalog (Moshir 1989). The first estimation of the temperature and radius of the disk was made by Fujiwara et al. (2013) using AKARI/IRC observations at 18 µm (Ishihara et al. 2010), on top of the previous Infrared Astronomical Satellite (IRAS) data as well as the Wide-field Infrared Survey Explorer (WISE) survey (Cutri et al. 2012). Moór et al. (2011) reported a fractional luminosity of the disk $f_{\rm disk} = L_{\rm disk}/L_\star = 4.8 \times 10^{-3}$ based on the SED.

2.3. Gas and dust detection with ALMA

The first millimeter detection was reported in Moór et al. (2017) with ALMA at 1.3 mm. The authors spatially resolved the disk in the continuum and detected spectrally resolved emission lines of several CO isotopologs, showing the presence of gas in the debris disk. They estimated the dust mass to be $1.4 \times 10^{-1}\,M_\oplus$ from the 1.3 mm observations. They also constrained the morphology of the ring from the continuum observations (but not for the gas), reporting an inclination of $37 \pm 13°$, a position angle of the major

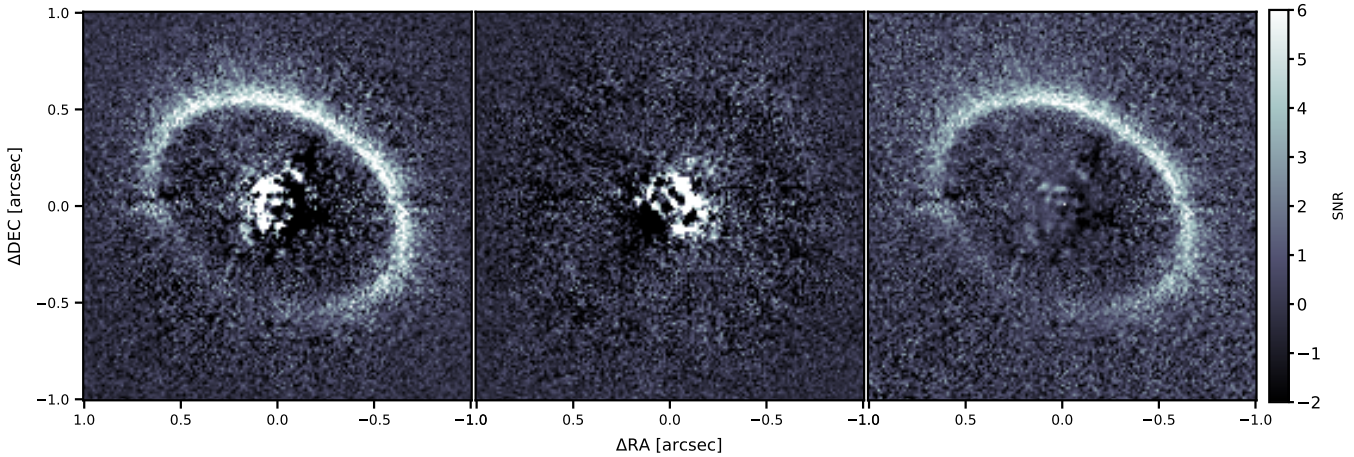

Fig. 1. Image of Q_ϕ, image of U_ϕ, and S/N map of the J band observations of HD 121617. North is up, east is left.

axis of $43 \pm 19°$, a diameter of 152 ± 15 au, and a radial thickness of 52 ± 17 au, which corresponds to the full width at half maximum (FWHM) of the 2D Gaussian used to model the ring (Moór et al. 2017). The ring size and thickness were corrected, according to the new distance of the star from *Gaia* DR3. As for the gas observations, using the standard isotopolog ratios of the local interstellar medium, they estimated a total ^{12}CO mass of $1.8 \times 10^{-2}\ M_\oplus$, which makes it part of the most massive gas disks detected so far in debris disk systems, with a gas-to-dust ratio of approximately 0.13.

3. Observations

3.1. SPHERE data

The HD 121617 star was observed with VLT/SPHERE (Beuzit et al. 2019) on the 28 April 2018 and 20 May 2018 with the same configuration[1]. Both epochs used the dual-beam polarimetric imaging mode (DPI; de Boer et al. 2020; van Holstein et al. 2020) of the Infra-Red Dual-band Imager and Spectrograph (IRDIS; Dohlen et al. 2008). The observations were done with the broadband J filter (BB_J; $\lambda_c = 1.245$ µm, $\Delta\lambda = 240$ nm, de Boer et al. 2020) and the N_ALC_YJH_S coronagraph mask with an inner working angle of 185 mas (Boccaletti et al. 2008). The pixel scale for this configuration was 12.26 mas per pixel (Maire et al. 2016). The observations were performed in field tracking mode, and an offset angle was applied in the derotator to avoid the loss of polarization, as described in de Boer et al. (2020).

The DPI mode of IRDIS allowed for the construction of the Stokes Q and U images. For this process, the light was split into two parallel beams that passed two linear polarizers with orthogonal transmissions and were imaged simultaneously on the same detector in the so-called left and right area. The subtraction of the images (left minus right) yielded four different $Q^\pm$ and $U^\pm$ images, depending on the angle orientation of the half-wave plate (HWP). When the HWP switch angle was 0°, the Q^+ image was formed. The HWP angles of 22.5°, 45°, and 65.5° respectively formed the images U^+, Q^-, and U^-. Finally, the Stokes Q and U images were used to construct the following equation:

$$X = \frac{1}{2}(X^+ - X^-), \tag{1}$$

where X equals U to reconstruct the Stokes U vector and X equals Q to reconstruct the Stokes Q vector. Thereby, a cycle of four HWP switch angles was necessary to obtain the Stokes U and Q vectors. More detailed explanations of this process can be found in de Boer et al. (2020) and van Holstein et al. (2020). A total of 24 HWP cycles were obtained (96 frames) for each epoch. The exposure time was set to 32 s to avoid saturation around the coronagraph and maximize the time of integration per frame, for a total integration time of 3072 s (51.2 min) for each epoch. The observation sequence was performed in the following order: First we acquired non-coronagraphic and non-saturated frames of the star (shifted out of the coronagraph by a few hundred mas for the flux calibration. Then, the star was moved back behind the coronagraph to perform frame centering with the "waffle" mode, a sinusoidal pattern put on the deformable mirror in order to create four symmetric spots. The intersection of the four spots gave, with a high accuracy, the position of the star behind the coronagraph. The science acquisition was then obtained with the polarimetric cycles described previously. At the end of the science sequence, another centering and flux calibration was performed in order to check the stability of the star centering and relative flux. Finally, a series of background calibrations were performed by pointing the telescope away from the star. Both observations were taken with good atmospheric conditions, with a seeing between 0.45″ and 0.75″ and a coherence time between 3 ms and 8.5 ms.

Data reduction was performed using the IRDIS Data reduction for Accurate Polarimetry (`IRDAP`[2]) pipeline (van Holstein et al. 2020). The pipeline includes background and flat-field calibrations, star centering, correction for instrumental polarization and polarization crosstalk, and the creation of the Stokes Q and U images. Then, `IRDAP` was used to construct the Q_ϕ and U_ϕ images (Schmid et al. 2006), which were used for further interpretation, following the definitions of de Boer et al. (2020):

$$\begin{aligned} Q_\phi &= -Q\cos 2\Phi - U\sin 2\Phi, \\ U_\phi &= +Q\sin 2\Phi - U\cos 2\Phi, \end{aligned} \tag{2}$$

where Φ is the position angle of the location of interest with respect to the stellar location. Figure 1 shows the final Q_ϕ and U_ϕ images obtained (the mean of the two epochs). The Q_ϕ image contains the polarimetric signal of the disk, revealing a bright and narrow ring. The ring shows a flux asymmetry between the northwest and the southeast sides. The U_ϕ image does not show any structured signal, which is expected for an optically thin disk (Canovas et al. 2015), and can therefore be used as a proxy

[1] ESO program ID: 0101.C-0420(A); PI: Johan Olofsson.

[2] https://irdap.readthedocs.io

Table 1. Photometric points for HD 121617.

Filter	Flux	Flux corr.	Error	$\lambda_{\rm eff}$	Ref.
–	(mJy)	(mJy)	(mJy)	(μm)	–
Tycho B	4372.0	5166.1	64.79	0.428	1
Gaia Gbp	3993.0	4577.1	37.59	0.504	2
Tycho V	4499.0	5111.1	48.14	0.534	1
Gaia G	3957.0	4440.2	36.39	0.586	2
Gaia Grp	3236.0	3506.8	30.53	0.769	2
2MASS *J*	2067.0	2143.2	58.18	1.235	3
2MASS *H*	1400.0	1431.8	60.48	1.662	3
2MASS *Ks*	883.0	896.1	15.97	2.159	3
WISE *W1*	409.0	411.8	14.73	3.35	4
WISE *W2*	240.0	241.0	7.56	4.60	4
WISE *W3*	72.2	72.3	3.14	11.56	4
WISE *W4*	567.0	567.2	31.28	22.09	4
PACS 100	961.8	961.8	24.25	97.90	5
PACS 160	415.4	415.4	17.17	153.95	5
ALMA	1.86	1.86	0.29	1330.0	6

Notes. The effective wavelengths $\lambda_{\rm eff}$ were taken from the Spanish Virtual Observatory Filter Profile Service (http://svo2.cab.inta-csic.es/theory/fps/) (Rodrigo et al. 2012; Rodrigo & Solano 2020). The "Flux corr." column corresponds to the flux corrected to the extinction described in Sect. 3.2.

References. (1) Høg et al. (2000), (2) Gaia Collaboration (2018), (3) Cutri et al. (2003), (4) Wright et al. (2010), (5) this work, and (6) Moór et al. (2017).

for uncertainties in the modeling of the observations. Figure 1 (right) shows the derived S/N map of Q_ϕ. Several artifacts remain in the Q_ϕ and U_ϕ reduced images. In the east part of both images (ΔRA = 0.5″, ΔDec = 0″), a horizontal artifact can be seen. This artifact, due to the SPHERE deformable mirror (fitting error; Cantalloube et al. 2019), is also present on the opposite side of the image, but less visible. Another artifact along the diagonal (from the top right to the bottom left) is present and is most likely due to the diffraction pattern of the VLT's spiders, which were not aligned with the Lyot stop in field tracking mode (low-order residuals; Cantalloube et al. 2019). Fortunately, the impact of these artifacts is small due to the brightness of the disk and the locations of the artifacts.

3.2. Photometry

Using the VO SED Analyzer (VOSA[3]; Bayo et al. 2008), we gathered the photometric observations from different missions and instruments to build the SED of HD 121617. To determine the stellar parameters (Sect. 2), we used the photometric measurements from TYCHO (B, V filters; Høg et al. 2000); *Gaia* (Gbp, *G* and Grp filters; Gaia Collaboration 2018); 2MASS (*J*, *H* and *Ks* filters; Cutri et al. 2003); and WISE (*W1* and *W2* filters; Wright et al. 2010). To fit the infrared excess (Sect. 5), we used WISE (*W3* and *W4* filters; Wright et al. 2010); *Herschel*/PACS (100 μm and 160 μm; this work); and the 1.3 mm ALMA observations (Moór et al. 2017). We corrected the photometry to the extinction estimated by *Gaia* (A_V = 0.134 mag, converted from A_0), assuming R_V = 3.25 from Gontcharov & Mosenkov (2018). We converted A_V to A_λ for each filter using the extinction law from Cardelli et al. (1989, Eqs. (1), (2), and (3)) for wavelengths below 3.3 μm, and the extinction law from Prato et al. (2003, $A_\lambda = (\frac{0.55}{\lambda[\mu m]})^{1.6} \times A_V$) for wavelengths larger than 3.3μm. The photometric points, corrected and not corrected for extinction, are presented in Table 1.

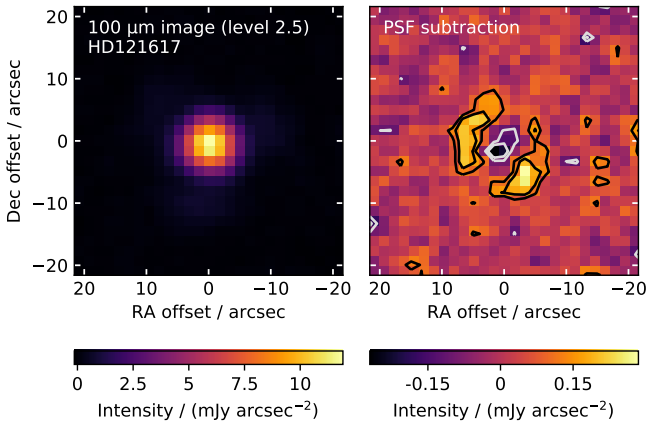

Fig. 2. Herschel/PACS observation of HD 121617 at 100 μm (left) and residual after a PSF subtraction performed with a calibration star (right). The continuum of the disk is marginally resolved.

The 100 μm PACS image is in fact marginally resolved. Figure 2 shows the data and a residual plot made by subtracting a point spread function (PSF) that was scaled to the image peak (where the PSF is an observation of the calibration star γ Dra). Fitting the residual image with a disk model (as in Yelverton et al. 2019) yields disk parameters that are consistent with those found in Sect. 4, but with significantly greater uncertainties, so we did not use this spatial information for any further analysis.

4. Morphological analysis of the SPHERE observations

4.1. Model and method

In order to constrain the disk morphology, we used the Debris DIsks Tool[4] (DDiT; Olofsson et al. 2020) to create synthetic models of the debris disk in polarized intensity. The DDiT was used with a Markov chain Monte Carlo (MCMC) code based on emcee[5] (Foreman-Mackey et al. 2013) to determine the best values of the tested parameters. The geometry of the disk is defined by the inclination i (0° for a face-on disk and 90° for an edge-on disk) and the position angle of the major axis with respect to the north ϕ. The dust density distribution of the disk is described in the radial r and vertical z directions as:

$$n(r,z) \propto \left[\left(\frac{r}{r_0}\right)^{-2\alpha_{\rm in}} + \left(\frac{r}{r_0}\right)^{-2\alpha_{\rm out}}\right]^{-1/2} \times {\rm e}^{-z^2/2h^2}, \quad (3)$$

with n as the dust grain volumetric density, r_0 as the reference radius of the disk, $\alpha_{\rm in}$ and $\alpha_{\rm out}$ as the inner and outer coefficients of the slope of the dust density distribution, and h as the scale height of the disk. In the case of a non-eccentric circular debris disk, r_0 is a constant equal to the semi-major axis a. For an eccentric orbit, r_0 is defined as:

$$r_0(\gamma) = \frac{a(1-e^2)}{1 + e\cos(\omega + \gamma)}, \quad (4)$$

with e as the eccentricity, ω as the argument of the pericenter, and γ as the azimuthal angle of the disk at r_0. Therefore, our

[3] http://svo2.cab.inta-csic.es/theory/vosa/

[4] https://github.com/joolof/DDiT

[5] https://emcee.readthedocs.io/en/stable/

Table 2. Priors and results of MCMC analysis.

Parameters	Priors	Best-fit value
a (au)	[75 ; 95]	78.6 ± 0.6
i (°)	[30 ; 60]	43.4 ± 0.8
ϕ (°)	[220 ; 260]	240.0 ± 0.9
g	[0 ; 0.9]	0.60 ± 0.04
$\alpha_{\rm in}$	[2 ; 35]	18.9 ± 2.3
$\alpha_{\rm out}$	[–15 ; –2]	-5.8 ± 0.4
e	[0, 0.1]	0.03 ± 0.01
ω (°)	[60 ; 200]	131.0 ± 15.1

Notes. a: semi-major axis. i: inclination. ϕ: position angle of the major axis of the disk with respect to the north. g: anisotropic scattering coefficient of the Henyey–Greenstien approximation for the dust. $\alpha_{\rm in}$ and $\alpha_{\rm out}$: respectively the inner and the outer slope of the power law distribution of the dust density. e: eccentricity. ω: argument of the pericenter. The "Best-fit" column was derived from the corner plot (Fig. B.1) of the MCMC analysis with 1-σ error.

fit allowed us to test whether the disk may be slightly eccentric. For the polarized scattering phase function, we used the Henyey–Greenstein approximation (Henyey & Greenstein 1941), which was parameterized with the coefficient g characterizing the scattering anisotropy of the dust (defined between −1, for backward scattering, and 1, for forward scattering) and the Rayleigh scattering function:

$$f_{\rm HG} = \frac{1-\cos^2(\theta)}{1+\cos^2(\theta)} \frac{1}{4\pi} \frac{1-g^2}{(1+g^2-2g\cos\theta)^{3/2}}, \quad (5)$$

where θ is the scattering angle (Engler et al. 2017; Olofsson et al. 2019). Finally, the aspect ratio, $\psi = \arctan(h/r)$, was fixed to 0.05 rad (Thébault 2009) due to the inclination of the disk, which is not adapted for a good estimation of ψ.

Priors for the eight free parameters of the MCMC run (a, i, ϕ, g, $\alpha_{\rm in}$, $\alpha_{\rm out}$, e, ω) are presented in Table 2. To compare each model to the data and determine the best value of the free parameters, we proceeded as follows: For each iteration of the MCMC run, the model was first convolved by a 2D normal distribution with a standard deviation of two pixels (corresponding to the FWHM of the off-axis image to avoid an additional source of noise). Then the flux of the model was scaled to best match the data, and the scaling factor $S_{\rm scale}$ was estimated as:

$$S_{\rm scale} = \frac{\sum \frac{I_{\rm data} \times I_{\rm model}}{\sigma^2}}{\sum \left(\frac{I_{\rm model}}{\sigma}\right)^2}, \quad (6)$$

with $I_{\rm data}$ as the 2D Q_ϕ image of the disk, $I_{\rm model}$ as the 2D synthetic Q_ϕ image of the disk, and σ as the noise map. This scaling was performed since `DDiT` produces images with no absolute flux for the reason that the latter depends on the total dust mass. We performed the minimization of the subtraction between the data and the model in an area including the disk and excluding the central part of the image where the residual starlight remains. We selected the area between 0.25″ and 1.1″ from the star position (respectively, 29 and 129 au in projected separation). In this way, we did not exclude the potential extended signal of the disk in the outer part. In the selected area, the χ^2 was computed as follows:

$$\chi^2 = \left(\frac{I_{\rm data} - S_{\rm scale} \times I_{\rm model}}{\sigma}\right)^2. \quad (7)$$

Finally, this χ^2 served as the log likelihood to the MCMC for the optimization of the free parameters. The MCMC was run with 80 walkers with a length of 500 and a burn-in fixed at 100 steps.

4.2. Noise map and uncertainties

The noise map σ was given by the U_ϕ image, which contains the same noise as the Q_ϕ image but without the astrophysical signal. To build the noise map, we computed the standard deviation per pixel in a small ring centered to the star. To account for the correlation between pixels, we added to the standard deviation an inflation term as described in Hinkley et al. (2021). This inflation term considers the spatial correlation of the PSF through the instrumental FWHM (40 mas or 3.3 pixels) and the radial elongation of the speckles due to the filter's bandwidth. Therefore the noise map was computed as:

$$\sigma(r) = \sqrt{FWHM \times r \times \frac{\Delta\lambda}{\lambda_{\rm c}}} \times \sigma_{\rm std}(r), \quad (8)$$

with r as the angular separation, $FWMH = 3.3$ pixels, $\Delta\lambda$ as the filter's bandwidth, $\lambda_{\rm c}$ as the central wavelength of the filter, and $\sigma_{\rm std}(r)$ as the radial standard deviation per pixel of the U_ϕ image. This is a conservative method that increases the uncertainties from the MCMC, which are usually underestimated. In addition, Langlois et al. (2021) gives the typical error on the star center for the SpHere INfrared survey for Exoplanets (SHINE), which is 1.5 mas (~0.18 au).

4.3. Results of the MCMC analysis

The results of the MCMC analysis are summarized in Table 2. The best-fit values were derived from the corner plots of the MCMC analysis, and their error bars are 1-σ of the corresponding probability density function (PDF) for each given parameter (Fig. B.1). Figure 3 shows the data, the best model, and the residual image. Since most of the signal from the disk is accounted for and therefore not visible in the residuals, our best-fit model can explain the observations.

The inner edge of the disk observed with SPHERE is far enough from the star as to not be affected by artifacts of residual light. Moreover, we used polarimetric observations, which do not necessitate post-processing techniques, such as ADI, and the results do not suffer from, for example, self-subtraction effects, as can be the case for total intensity images. Therefore, we improved the constraints on the geometry of the disk compared to previous ALMA studies (Moór et al. 2017). The SPHERE and ALMA results are compatible, as we found a semi-major axis of 78.6 ± 0.6 au (vs. 76 ± 8 au), an inclination of $43.4 \pm 0.7°$ (vs. $37 \pm 13°$), and a position angle of the major axis of $240.0 \pm 0.9°$ (vs. $223 \pm 19°$). However, the ring observed with SPHERE appeared much narrower compared to the ring observed with ALMA. The equivalent FWHM of the disk in the SPHERE image is around 23 au (0.2″), while Moór et al. (2017) reported an FWHM of 52 ± 17 au (0.44″). The difference can be explained by the larger angular beam size of the ALMA observations (~0.5″) so that the millimeter-dust ring is not resolved. Nonetheless, the angular resolution of 0.03″ in the SPHERE observations, allows us to resolve the ring's width.

We found that the shape of the dust density distribution for the inner edge of the ring is extremely steep, with a power law slope $\alpha_{\rm in} = 18.9 \pm 2.3$. The outer edge of the ring is also

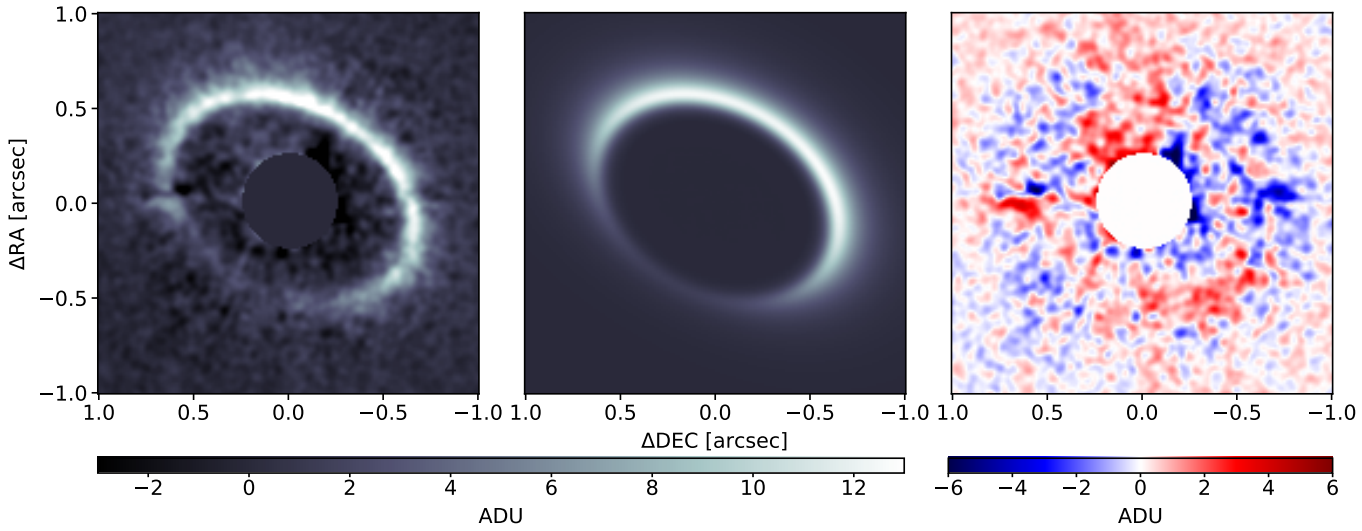

Fig. 3. Image of Q_ϕ, best model, and residual image after subtraction of the best model from the Q_ϕ image. The gray area in the middle of each image is a numerical mask used to exclude the residual starlight.

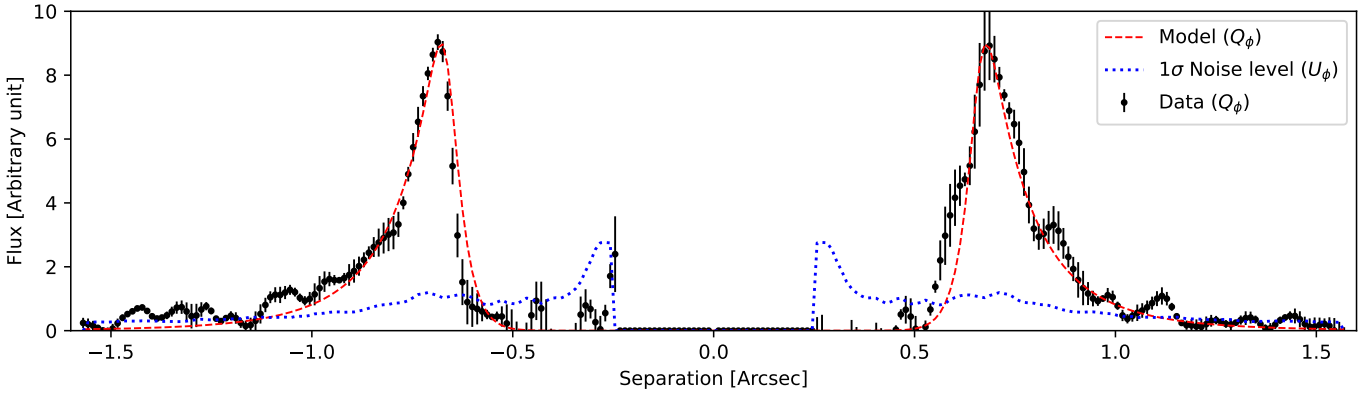

Fig. 4. Radial profile of Q_ϕ following the projected major axis (6 pixels wide) from the southwest to the northeast of the disk is shows with a black points and with the corresponding error bars. The radial profile of the best model is shown with a red dashed line, and the noise level obtained with the azimuthal standard deviation of the U_ϕ image is shown with a blue dotted line.

steeper than the expected dust density distribution for an evolved debris disk (Thébault & Wu 2008), with a power law slope $\alpha_{\rm out} = -5.8 \pm 0.4$ instead of the typical $\alpha_{\rm out} = -1.5$. In Fig. 4, we show the radial profiles along the major axis for the northeast and southwest directions, compared to the radial profile of the best model and the 1σ noise level from the U_ϕ image. Radial profiles were obtained by averaging a band six pixels wide along the major axis.

Finally, our analysis also shows that the disk is slightly eccentric, with an eccentricity of 0.03 ± 0.01. With a semi-major axis of 78.6 ± 0.6 au, this eccentricity leads to an apocenter at 81.0 ± 1.4 au and a pericenter at 76.2 ± 1.4 au from the star, with the argument of the pericenter being at $131.0 \pm 15.1°$.

5. SED modeling

Our analysis made with `DDiT` was focused on the disk morphology. In this section, we use the previously constrained parameters to estimate the dust properties. This is indeed a good way to proceed because SED fitting is a degenerate problem where the radial distance of the belt and the minimum grain size are correlated with each other. But once the belt location is fixed, we can directly constrain the grain properties.

5.1. SED with `MCFOST`

A 3D radiative transfer code for circumstellar disks, `MCFOST`[6] (Pinte et al. 2006, 2009) is able to produce synthetic SED, images, or absorption lines for specific systems. The code was initially developed for protoplanetary disks (optically thick, with gas in local thermal equilibrium, or not) but is also suitable for optically thin debris disks. We used `MCFOST` to compute the SED of HD 121617 with the aim of constraining the following dust parameters: the dust mass $M_{\rm dust}$, the minimum grain size radius $s_{\rm min}$, and the power law of the grain size distribution q. In `MCFOST`, stellar parameters are defined by the Kurucz model (Castelli & Kurucz 2003), which corresponds the most to the SED. Our selected model is the Kurucz model at $T_{\rm eff}$ = 9500 K, $\log g$ = 5.0, and with the assumption of solar metallicity. The procedure to determine this model is presented in Appendix A. The disk morphology was defined by the results of the MCMC analysis of Sect. 4 (though we assumed a disk

[6] https://github.com/cpinte/mcfost

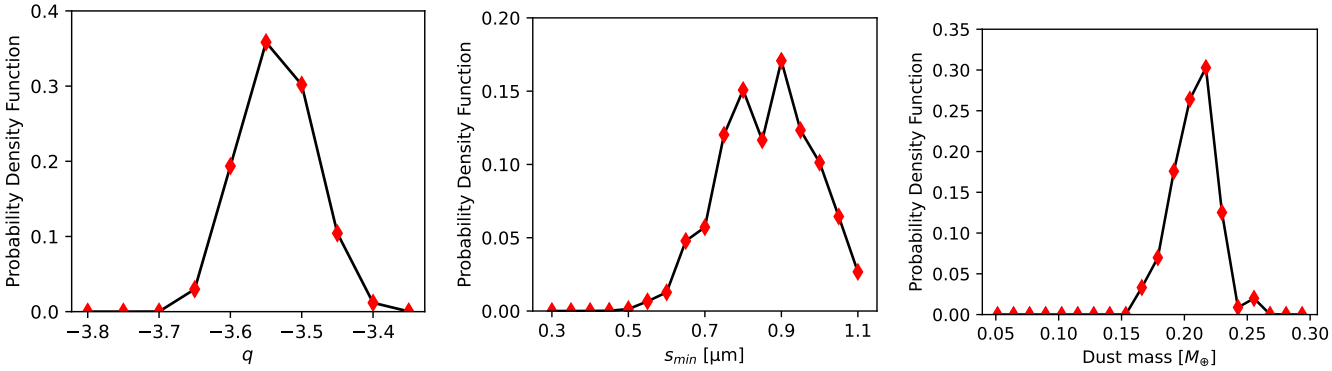

Fig. 5. Probability density function for q, $s_{\rm min}$ and $M_{\rm dust}$.

with zero eccentricity): $a = 78.6$ au, $i = 43.4°$, $\phi = 240.0°$, $\alpha_{\rm out} = -5.8$, and $\alpha_{\rm in} = 18.9$. For the sake of simplicity and given the small eccentricity (~0.03), we fixed the eccentricity to zero. For the grain properties, we used the Mie theory (i.e., compact spherical grains) with a maximum grain size radius $s_{\rm max} = 1000$ µm, and we used the optical constant of astrosilicate grains (Draine & Lee 1984). Several studies of HR 4796 show that Mie theory is not always adapted to describe the dust grain geometry (Perrin et al. 2015; Milli et al. 2019). However, the measurement of the scattering phase function of a total intensity observation is required to constrain the dust grain geometry, in addition to the scattering phase function in polarimetry. Unfortunately, the total intensity is not yet available for HD 121617.

Subsequently, MCFOST was used to produce a synthetic SED of the system with a log-spaced sampling of 300 wavelengths from 0.1 µm to 1500 µm. This synthetic SED was ultimately converted into synthetic photometric points for specific filters for comparison with photometric data. We proceeded using MCFOST in the non-LTE configuration. Since the disk should be optically thin, the infrared flux scales linearly with the total dust mass. Therefore, we fixed the dust mass and afterwards found the scaling factor $S_{\rm flux}$ that minimizes the residuals. A posteriori, we checked that the best-fit solution indeed remains in the optically thin regime at all wavelengths with $\tau = 0.19$ at 1245 µm in the mid plane. The scaling factor $S_{\rm flux}$ was computed as:

$$S_{\rm flux} = \frac{\sum_{\lambda} \frac{F_{\rm disk}(\lambda)}{\sigma(\lambda)^2}[F_{\rm obs}(\lambda) - F_{\rm star}(\lambda)]}{\sum_{\lambda} \frac{F_{\rm disk}(\lambda)^2}{\sigma(\lambda)^2}}, \quad (9)$$

where $F_{\rm obs}(\lambda)$ is the observed flux for the λ filter and $\sigma(\lambda)$ is the observed flux error for the λ filter. Respectively, $F_{\rm disk}(\lambda)$ and $F_{\rm star}(\lambda)$ are the synthetic flux of the disk component and the star component for the λ filter from MCFOST.

To determine the best values of $s_{\rm min}$ and q, they were sampled into a grid of values (Table 3). The χ^2 was computed with the infrared photometry in the same way as for the star parameters analysis in Sect. 2 and included the following filters: WISE $W3$, WISE $W4$, PACS 100, PACS 160, and the ALMA observation at 1.33 mm. We did not consider filters below 10 µm because the disk contribution at those wavelengths is negligible compared to that of the star.

5.2. Results

Table 3 shows the results of the analysis with MCFOST with values for the best-fit model (Fig. 6) derived from the PDF shown in Fig. 5. The central value was understood to be obtained when the cumulated PDF reached 50% of the maximum, while the error bars are for 16% and 84%, respectively. We found $s_{\rm min} = 0.87^{+0.12}_{-0.13}$ µm, $q = -3.53 \pm 0.05$, and $M_{\rm dust} = 0.21 \pm 0.02\, M_\oplus$. As the dust mass was fixed via scaling to the SED, we could not directly compute the PDF for the mass. Instead, we randomly sampled the output distribution of $M_{\rm dust}$ to produce a homogeneous grid of values suitable to produce a PDF. This operation was repeated 1000 times for averaging purposes. The results are discussed in the next section.

Table 3. Parameters and results of the MCFOST analysis.

Parameter	Interval	Step	Best-fit model
$s_{\rm min}$ (µm)	[0.30, 1.10]	0.05	$0.87^{+0.12}_{-0.13}$
q	[−3.8, −3.35]	0.05	-3.53 ± 0.05
$M_{\rm dust}$ ($M_\oplus$)	[0.27]	– [(a)]	0.21 ± 0.02

Notes. [(a)]The dust mass $M_{\rm dust}$ has only an initial mass and does not have a step value due to the method used to compute it.

6. Discussion

6.1. Radial profile

Our results led to a high value of $\alpha_{\rm in} = 18.9$, corresponding to a very sharp inner edge of the disk. Such sharp inner edges have been witnessed around several other systems (see Table E.1 in Adam et al. 2021) and would indicate that "something" is shaping them – the most likely explanation being that a sharp inner edge corresponds to the outer limit of the chaotic region surrounding a yet-undetected planet just located inward of the belt (e.g., Lagrange et al. 2012). We note that, contrary to outer edges, radiation pressure or stellar wind do not place small grains in the dynamically "forbidden" region inward of the inner edge, which probably explains why sharp inner edges are more commonly observed than sharp outer ones (Adam et al. 2021). Poynting-Robertson drag could make small grains spiral inward, which could also smooth out the sharpness of an inner disk edge, but the fraction of grains that can escape the main belt this way should be negligible for a very bright and collisionally active disk such as HD 121617 (Wyatt 2005).

For the outer edge of the disk radial profile, we got $\alpha_{\rm out} = -5.8$, corresponding to a slope for the radial surface density profile in −4.8. This is more than the canonical slope in −1.5 (or in −3.5 for the flux) that is expected in the outer regions

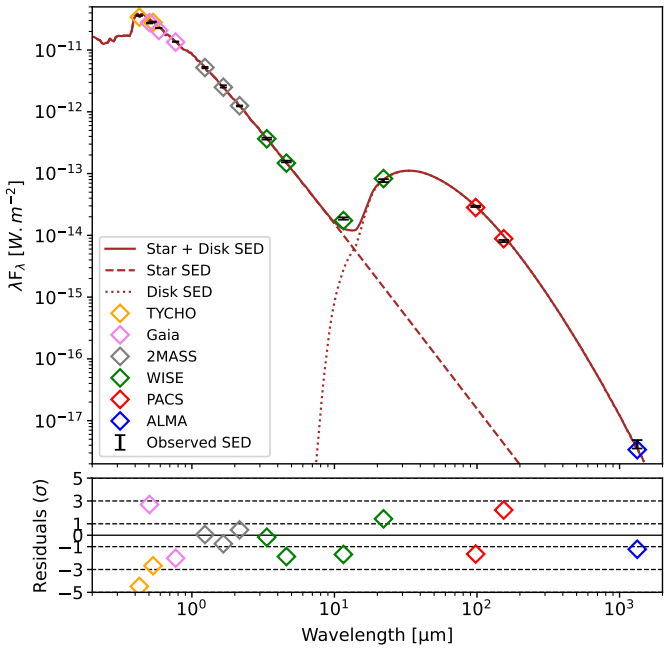

Fig. 6. SED of the HD 121617 system (top) and the residuals after subtraction of the best-fit model (bottom). The best model of the star is represented by the brown dashed line, that of the disk by the brown dotted line, and their sum is the brown solid line. The photometric points with their error bars are represented by vertical black symbols. Synthetic photometric points are represented by diamonds. The color of the diamonds corresponds to the instrument used for the observations.

beyond a collision-dominated belt of parent bodies under the competing effects of collisional activity within the belt and radiation pressure (or stellar wind), placing small grains on highly eccentric orbits outside of the belt (Strubbe & Chiang 2006; Thébault & Wu 2008). We note, however, that this −1.5 slope is not supposed to be reached immediately beyond the main belt but after a transition region of relative width $\Delta r/r_0 \sim 0.2$–0.3, where the radial profile can be significantly steeper (Thébault et al. 2012, 2014). In the present case, the radial profile is constrained out to 1.1″, after which the noise begins to dominate the signal (Fig. 4), which is approximately 40% outside of the peak radial location. This is slightly more than the theoretical width of the "natural" transition region beyond a collisional belt and could thus be interpreted as the signature of some additional removal process, such as dynamical perturbations by a planet or a stellar companion (Thébault 2012; Lagrange et al. 2012). Another possible explanation for a sharp density drop beyond a belt of parent bodies could be that the belt is dynamically "cold", that is, it has a low collisional activity that creates a dearth of small grains with respect to larger ones (Thébault & Wu 2008). However, this scenario appears unlikely in the present case given the very high fractional luminosity ($\sim 4.8 \times 10^{-3}$) of the disk, which should indicate a high level of dustiness. At any rate, future observations constraining the disk's radial profile farther away from the main belt would greatly benefit our understanding of both the inner and outer edges and the potential presence of planets just inside or outside of it (e.g., observations with the *James Webb* Space Telescope).

6.2. Dust mass

In debris disks, the bulk of the mass is carried by large bodies that cannot be seen with the full SED nor in the sub-millimeter. However, we have access to the dust mass via millimeter-observations.

We find the value of $M_{\rm dust} = 0.21\,M_\oplus$ is slightly higher than the dust mass obtained by Moór et al. (2017) from the flux density at 1.3 mm, $0.12\,M_\oplus$[7]. The difference between the two values is likely due to the fact that we used the whole SED to compute the mass, whereas the value from the other study is only based on the 1.3 mm flux. Moreover, we used slightly different assumptions for the dust composition and opacities, which can lead to these kinds of differences. However, the differences are relatively limited, and our $M_{\rm dust}$ value remains compatible with previous estimates.

6.3. Size distribution and smallest grains

The best-fit value found for q, the power law of the grain size distribution, is −3.53. This value is remarkably close to the canonical value of −3.5 expected for infinite self-similar collisional cascades at steady state (Dohnanyi 1969) and is fully compatible with the size distribution profiles found in more realistic numerical explorations of collisional debris disks (Thébault & Augereau 2007; Kral et al. 2013)[8].

As for the minimum grain size, we found $s_{\rm min} = 0.87$ µm. It is useful to compare this value to the blowout size, $s_{\rm blow}$, corresponding to the grain size for which the ratio, β, between the radiation pressure ($F_{\rm rad}$) and the gravitation force ($F_{\rm grav}$) is equal to 0.5. Grains smaller than $s_{\rm blow}$ that are produced from parent bodies on circular orbits are ejected out of the system due to radiation pressure. The β ratio is defined by:

$$\beta = 0.5738 Q_{\rm pr} \left(\frac{1\ {\rm g\,cm^{-3}}}{\rho_{\rm d}}\right)\left(\frac{1\ {\rm \mu m}}{s}\right)\frac{L/L_\odot}{M/M_\odot}, \quad (10)$$

where L is the stellar luminosity, G is the gravitational constant, M is the stellar mass, c is the speed of light, $Q_{\rm pr}$ is the radiation pressure efficiency averaged over the stellar spectrum, and $\rho_{\rm d}$ is the dust density. We assumed $Q_{\rm pr} = 1$ for geometric optics approximation and $\rho_{\rm d} = 3.3\ {\rm g\,cm^{-3}}$ for typical astrosilicate grains (Krivov et al. 2009). With the stellar parameters from Appendix A, we obtained $s_{\rm blow} = 2.91$ µm, which is approximately three times larger than $s_{\rm min}$.

We cannot rule out that this difference is due to assumptions made about the grain geometry, such as $Q_{\rm pr} = 1$, or chemical composition (pure astrosilicates). Pawellek & Krivov (2015) show indeed that these parameters can have an important contribution to the blowout size. For astrosilicate in particular, the value of $Q_{\rm pr}$ varies between two and 0.2 as a function of the wavelength (Pawellek & Krivov 2015, Fig. 2). However, other dust compositions (such as carbon, ice, or a mix) have lower dust densities, implying a higher blowout size.

If the discrepancy between $s_{\rm blow}$ and $s_{\rm min}$ is real, then HD 121617 would join a handful of systems, such as HD 32297, AU Mic, HD 15115, or HD 61005 (Thébault & Kral 2019), for which a significant presence of grains with $\beta > 0.5$ has been inferred. Such a presence has often been interpreted as being due to violent and/or transient events, such as the catastrophic breakup of a large planetesimal (Johnson et al. 2012; Kral et al. 2015) or a so-called collisional avalanche (Grigorieva et al. 2007;

[7] We applied the correction of the distance to the initial value obtained by Moór et al. (2017), $1.4 \times 10^{-1}\,M_\oplus$.

[8] Given the simplicity of the present analysis, we chose to ignore more complex features found in realistic size distributions, such as wavy patterns.

Thébault & Kral 2018), with the caveat that such events might be short lived and statistically unlikely. However, the numerical exploration of Thébault & Kral (2019) has shown that for bright disks around A stars, there is a significant population of $s < s_{\rm blow}$ grains, even for a "standard" debris disk at collisional steady state. The HD 121617 star, with a $f_{\rm d} = 4.8 \times 10^{-3}$ disk around an A1V central star, would fit nicely into this category.

Another possible explanation for the presence of small $\beta > 0.5$ particles could be the effect of the gas that has been unambiguously detected in this system. Gas drag could indeed slow down the outward motion of unbound grains (Bhowmik et al. 2019) and push small micron-sized bound grains in regions where collisional activity is lower and lifetimes are longer (Olofsson et al. 2022). This potential effect of gas on the observed dust, which could also affect the profile of the belt's inner and outer edges, is discussed in more detail in the next subsection.

6.4. Effect of gas on the dust grains

The results we have obtained so far do not necessarily require the presence of gas to be explained, but we note that large amounts of CO ($\sim 2 \times 10^{-2}\,M_\oplus$) are present in the system (Moór et al. 2017), which may lead to gas drag of the smallest dust grains (Takeuchi & Artymowicz 2001). To verify this, we calculated the stopping time of the grains of size s of bulk density $\rho_{\rm d}$ located in a disk at 78 au of radial extent ΔR and bathed in a total mass of gas $M_{\rm gas}$, which leads to

$$T_{\rm s} \sim 6 \left(\frac{\rho_{\rm d}}{2\,{\rm g\,cm^{-3}}}\right)\left(\frac{s}{1\,\mu{\rm m}}\right)\left(\frac{M_{\rm gas}}{2\times10^{-2}\,M_\oplus}\right)^{-1}\left(\frac{\Delta R}{50\,{\rm au}}\right). \quad (11)$$

A particle with a stopping time close to one orbital period would react to gas in about one dynamical timescale (the dust grain is said to be marginally coupled). Therefore, we find that the smallest grains in the system (~1 µm) can begin to respond to the presence of gas within tens of orbital timescales considering only CO is present. In the presence of radiation pressure, these grains are expected to move slowly outward (e.g., Takeuchi & Artymowicz 2001). The final parking location of these grains is where $\beta = \eta$, where η is related to the gas pressure gradient and sets the gas velocity to $v_{\rm k}\sqrt{1-\eta}$ ($v_{\rm k}$ being the Keplerian velocity). However, the grains can be destroyed by collisions more quickly than they are able reach this parking location, depending on the mass of gas and the density of the dust disk (Olofsson et al. 2022). Overall, the surface brightness radial slope is expected to be shallower than usual (i.e., closer to –2 than –3.5) in the halo beyond the disk. Before reaching this halo-like slope, there is an abrupt transition where the planetesimal belt stops, leading to surface brightness slopes <–5 over short radial distances. However, this is true even in cases where no gas is present (Thébault & Augereau 2007). Although the abrupt transition can be observed with SPHERE, the halo is diluted by noise, and its radial slope cannot be calculated from current observations. Our main conclusion is that, even though gas is expected to be able to drag the smallest grains, its effects are not detectable on the radial profiles from current observations.

It is expected that CO will photodissociate and create some carbon and oxygen. Depending on the amount of shielding and the viscosity of the gas disk, the number densities of carbon and oxygen may exceed that of CO (e.g., Kral et al. 2019). In the case where there is much more mass than $\sim 2 \times 10^{-2}\,M_\oplus$ (e.g., carbon and oxygen dominate), we still expect the same general conclusion on the radial profile (even if H_2 dominates, i.e., primordial origin). The main difference would be that small grains would move outward more quickly and have a better chance of reaching their parking place before being destroyed by collisions. However, one major difference is in the vertical profile of the grains in the case of low gas masses where CO dominates the gas mass. In such cases, vertical settling should only be significant for the smallest grains observed in scattered light, but this is difficult to spot in an inclined system (Olofsson et al. 2022). For more massive gas disks, the larger grains would have time to settle, creating needle-like disks in the sub-millimeter as well (Olofsson et al. 2022). This difference would be easier to spot in an edge-on system but is difficult given the geometry of the disk around HD 121617.

Finally, one may wonder whether a steep inner edge may be explained by the presence of gas. As stated in Sect. 6.1, many disks observed in scattered light have steep inner edges and no detected gas, and other causes, such as the presence of a planet (see Sect. 6.1), provide a good explanation for the origin of such edges. However, we note that gas helps shape the steep inner edge, as the smallest micron-sized grains observed in scattered light would be pushed outward on approximately ten dynamical timescales (see Eq. (11)), which is to be compared to the timescale for refilling them, the collisional timescale. For the smallest grains, the collision timescale can be approximated by $(\tau\Omega)^{-1}$, which corresponds to 200 dynamical timescales, given the optical depth $\tau \sim 5\times10^{-3}$. The order of magnitude difference between the two timescales means that the smallest micron-sized grains would be slightly depleted in the innermost region, which cannot be refilled by grains coming from closer regions. Finer observations and numerical simulations dealing with both dynamics and collisions in the presence of gas would be needed to draw more solid conclusions as to whether gas drag can really create steeper inner edges.

7. Conclusion

Using the polarimetric mode of the VLT/SPHERE-IRDIS instrument, we resolved the gas-rich debris disk around the star HD 121617 for the first time in scattered light. The observations used in this study were made in 2018 using the dual-beam polarimetric imaging mode in the *J* band with a corresponding angular resolution of 0.03″ (or ~3.5 au), an order of magnitude better than previous ALMA observations in the millimeter (Moór et al. 2017).

The high contrast of the images coupled with their high angular resolution allowed us to significantly improve the previous constraints on the disk morphology. We fit the image using a disk located at a semi-major axis a, with an inclination i, and with an eccentricity e and a density made up of two power laws, $\alpha_{\rm in}$ and $\alpha_{\rm out}$. Using the radiative transfer code `DDiT` in an MCMC fashion, we find that the best fit is $a = 78.6 \pm 0.6$ au, $i = 43.4 \pm 0.8°$, $e = 0.03 \pm 0.01$, $\alpha_{\rm in} = 18.9 \pm 2.3$, and $\alpha_{\rm out} = -5.8 \pm 0.4$. We also constrained the position angle of the major axis to $\phi = 240.0 \pm 0.9°$, the anisotropic scattering coefficient to $g = 0.60 \pm 0.04$ (if positive), and the argument of pericenter (if eccentric) to $\omega = 131.0 \pm 15.1°$.

Taking advantage of these new geometric constraints to mitigate degeneracies in the SED fitting process, we derived the dust properties by fitting the full SED of the system. We find that the minimum grain size is best fitted by $s_{\rm min} = 0.87^{+0.12}_{-0.13}$ µm, a value that appears smaller than the blowout size. If real, it

would not be surprising, as the disk around HD 121617 has a very high fractional luminosity, close to 5×10^{-3}, and in this case, an overabundance of small unbound grains of submicron size is expected (Thébault & Kral 2019). The presence of large amounts of gas, as in this system, may also be able to slow down these unbound grains, which can then cause them to accumulate even more (e.g., Bhowmik et al. 2019). The SED fit also leads to a size distribution slope $q = -3.53 \pm 0.05$, which is naturally expected in a collision-dominated debris disk (e.g., Thébault & Augereau 2007; Kral et al. 2013). Finally, we constrained the dust mass to $M_{\rm dust} = 0.21 \pm 0.02\, M_{\oplus}$.

One of the main constraints on the disk morphology is that the density profile of the inner edge is radially very steep (power law in $\sim r^{20}$), which could be due to the presence of a yet unseen planet near the inner edge of the disk. We also note that, qualitatively, the presence of gas in this system could be the reason for the sharp inner edge of the dust profile. The outer edge is also sharper than predicted by steady-state models of debris disk halos, but our constraint should be taken with caution, as it only concerns the very early parts of the halo (up to 1.1″) where a sharp transition region is naturally expected. Further observations targeting the halo at larger distances (e.g., with JWST) would be needed to infer the presence of a planet or to see the effect of gas on the outer profile of the surface brightness at large distances, which is expected to be shallower than –3.5 and closer to –2 (Olofsson et al. 2022).

Acknowledgements. C.P. acknowledges support by the French National Research Agency (ANR Tremplin-ERC: ANR-20-ERC9-0007 REVOLT). C.P. also acknowledges financial support from Fondecyt (grant 3190691). J.O. acknowledges financial support from Fondecyt (grant 1180395). M.M. acknowledges financial support from Fondos de Investigación 2022 de la Universidad Viña del Mar. G.M.K. was supported by the Royal Society as a Royal Society University Research Fellow. C.P., J.O., M.M., A.B. and D.I. acknowledge support by ANID, – Millennium Science Initiative Program – NCN19_171. This publication makes use of VOSA, developed under the Spanish Virtual Observatory (https://svo.cab.inta-csic.es) project funded by MCIN/AEI/10.13039/501100011033/ through grant PID2020-112949GB-I00. VOSA has been partially updated by using funding from the European Union's Horizon 2020 Research and Innovation Programme, under Grant Agreement no. 776403 (EXOPLANETS-A). This research has made use of the SVO Filter Profile Service (http://svo2.cab.inta-csic.es/theory/fps/) supported from the Spanish MINECO through grant AYA2017-84089. This work has made use of data from the European Space Agency (ESA) mission *Gaia* (https://www.cosmos.esa.int/gaia), processed by the *Gaia* Data Processing and Analysis Consortium (DPAC, https://www.cosmos.esa.int/web/gaia/dpac/consortium). Funding for the DPAC has been provided by national institutions, in particular the institutions participating in the *Gaia* Multilateral Agreement. We thank the referee for their helpful comments.

References

Adam, C., Olofsson, J., van Holstein, R. G., et al. 2021, A&A, 653, A88
Arriaga, P., Fitzgerald, M. P., Duchêne, G., et al. 2020, AJ, 160, 79
Bayo, A., Rodrigo, C., Barrado Y Navascués, D., et al. 2008, A&A, 492, 277
Beuzit, J. L., Vigan, A., Mouillet, D., et al. 2019, A&A, 631, A155
Bhowmik, T., Boccaletti, A., Thébault, P., et al. 2019, A&A, 630, A85
Boccaletti, A., Abe, L., Baudrand, J., et al. 2008, SPIE Conf. Ser., 7015, 70151B
Boccaletti, A., Sezestre, E., Lagrange, A. M., et al. 2018, A&A, 614, A52
Canovas, H., Ménard, F., de Boer, J., et al. 2015, A&A, 582, A7
Cantalloube, F., Dohlen, K., Milli, J., Brandner, W., & Vigan, A. 2019, The Messenger, 176, 25
Cardelli, J. A., Clayton, G. C., & Mathis, J. S. 1989, ApJ, 345, 245
Castelli, F., & Kurucz, R. L. 2003, in Modelling of Stellar Atmospheres, 210, eds. N. Piskunov, W. W. Weiss, & D. F. Gray, A20
Cotten, T. H., & Song, I. 2016, ApJS, 225, 15
Crotts, K. A., Matthews, B. C., Esposito, T. M., et al. 2021, ApJ, 915, 58
Cutri, R. M., Skrutskie, M. F., van Dyk, S., et al. 2003, 2MASS All Sky Catalog of Point Sources
Cutri, R. M., Wright, E. L., Conrow, T., et al. 2012, Explanatory Supplement to the WISE All-Sky Data Release Products, Explanatory Supplement to the WISE All-Sky Data Release Products
de Boer, J., Langlois, M., van Holstein, R. G., et al. 2020, A&A, 633, A63
Dohlen, K., Langlois, M., Saisse, M., et al. 2008, SPIE Conf. Ser., 7014, 70143L
Dohnanyi, J. S. 1969, J. Geophys. Res., 74, 2531
Draine, B. T., & Lee, H. M. 1984, ApJ, 285, 89
Engler, N., Schmid, H. M., Thalmann, C., et al. 2017, A&A, 607, A90
Esposito, T. M., Kalas, P., Fitzgerald, M. P., et al. 2020, AJ, 160, 24
Feldt, M., Olofsson, J., Boccaletti, A., et al. 2017, A&A, 601, A7
Ford, H. C., Clampin, M., Hartig, G. F., et al. 2003, SPIE Conf. Ser., 4854, 81
Foreman-Mackey, D., Hogg, D. W., Lang, D., & Goodman, J. 2013, PASP, 125, 306
Fujiwara, H., Ishihara, D., Onaka, T., et al. 2013, A&A, 550, A45
Gagné, J., Roy-Loubier, O., Faherty, J. K., Doyon, R., & Malo, L. 2018, ApJ, 860, 43
Gaia Collaboration 2018, VizieR Online Data Catalog: I/345
Gaia Collaboration (Prusti, T., et al.) 2016, A&A, 595, A1
Gaia Collaboration (Schultheis, M., et al.) 2023, A&A, in press, DOI https://doi.org/10.1051/0004-6361/202243283
Gontcharov, G. A., & Mosenkov, A. V. 2018, MNRAS, 475, 1121
Grigorieva, A., Artymowicz, P., & Thébault, P. 2007, A&A, 461, 537
Henyey, L. G., & Greenstein, J. L. 1941, ApJ, 93, 70
Hinkley, S., Matthews, E. C., Lefevre, C., et al. 2021, ApJ, 912, 115
Høg, E., Fabricius, C., Makarov, V. V., et al. 2000, A&A, 355, A27
Hoogerwerf, R. 2000, MNRAS, 313, 43
Houk, N. 1978, Michigan Catalogue of Two-dimensional Spectral Types for the HD Stars
Hughes, A. M., Lieman-Sifry, J., Flaherty, K. M., et al. 2017, ApJ, 839, 86
Hughes, A. M., Duchêne, G., & Matthews, B. C. 2018, ARA&A, 56, 541
Ishihara, D., Onaka, T., Kataza, H., et al. 2010, A&A, 514, A1
Johnson, B. C., Lisse, C. M., Chen, C. H., et al. 2012, ApJ, 761, 45
Jovanovic, N., Martinache, F., Guyon, O., et al. 2015, PASP, 127, 890
Kóspál, Á., Moór, A., Juhász, A., et al. 2013, ApJ, 776, 77
Kral, Q., Thébault, P., & Charnoz, S. 2013, A&A, 558, A121
Kral, Q., Thébault, P., Augereau, J. C., Boccaletti, A., & Charnoz, S. 2015, A&A, 573, A39
Kral, Q., Wyatt, M., Carswell, R. F., et al. 2016, MNRAS, 461, 845
Kral, Q., Marino, S., Wyatt, M. C., Kama, M., & Matrà, L. 2019, MNRAS, 489, 3670
Krivov, A. V., & Wyatt, M. C. 2021, MNRAS, 500, 718
Krivov, A. V., Herrmann, F., Brandeker, A., & Thébault, P. 2009, A&A, 507, 1503
Lagrange, A. M., Milli, J., Boccaletti, A., et al. 2012, A&A, 546, A38
Lagrange, A. M., Langlois, M., Gratton, R., et al. 2016, A&A, 586, L8
Langlois, M., Gratton, R., Lagrange, A. M., et al. 2021, A&A, 651, A71
Lee, E. J., & Chiang, E. 2016, ApJ, 827, 125
Macintosh, B., Graham, J. R., Ingraham, P., et al. 2014, PNAS, 111, 12661
Maire, A.-L., Langlois, M., Dohlen, K., et al. 2016, SPIE Conf. Ser., 9908, 990834
Mannings, V., & Barlow, M. J. 1998, ApJ, 497, 330
Marois, C., Lafrenière, D., Doyon, R., Macintosh, B., & Nadeau, D. 2006, ApJ, 641, 556
Matrà, L., Marino, S., Kennedy, G. M., et al. 2018, ApJ, 859, 72
Matrà, L., Wyatt, M. C., Wilner, D. J., et al. 2019, AJ, 157, 135
Milli, J., Mouillet, D., Lagrange, A. M., et al. 2012, A&A, 545, A111
Milli, J., Engler, N., Schmid, H. M., et al. 2019, A&A, 626, A54
Moór, A., Ábrahám, P., Juhász, A., et al. 2011, ApJ, 740, L7
Moór, A., Curé, M., Kóspál, Á., et al. 2017, ApJ, 849, 123
Moór, A., Kral, Q., Ábrahám, P., et al. 2019, ApJ, 884, 108
Moshir, M. 1989, IRAS Faint Source Survey, Explanatory Supplement Version 1 and Tape
Nakatani, R., Kobayashi, H., Kuiper, R., Nomura, H., & Aikawa, Y. 2021, ApJ, 915, 90
Olofsson, J., Samland, M., Avenhaus, H., et al. 2016, A&A, 591, A108
Olofsson, J., van Holstein, R. G., Boccaletti, A., et al. 2018, A&A, 617, A109
Olofsson, J., Milli, J., Thébault, P., et al. 2019, A&A, 630, A142
Olofsson, J., Milli, J., Bayo, A., Henning, T., & Engler, N. 2020, A&A, 640, A12
Olofsson, J., Thébault, P., Kral, Q., et al. 2022, MNRAS, 513, 713
Pawellek, N., & Krivov, A. V. 2015, MNRAS, 454, 3207
Pawellek, N., Wyatt, M., Matrà, L., Kennedy, G., & Yelverton, B. 2021, MNRAS, 502, 5390
Pecaut, M. J., & Mamajek, E. E. 2016, MNRAS, 461, 794

Perrin, M. D., Duchene, G., Millar-Blanchaer, M., et al. 2015, ApJ, 799, 182
Perrot, C., Boccaletti, A., Pantin, E., et al. 2016, A&A, 590, A7
Perrot, C., Thebault, P., Lagrange, A.-M., et al. 2019, A&A, 626, A95
Pinte, C., Ménard, F., Duchêne, G., & Bastien, P. 2006, A&A, 459, 797
Pinte, C., Harries, T. J., Min, M., et al. 2009, A&A, 498, 967
Prato, L., Greene, T. P., & Simon, M. 2003, ApJ, 584, 853
Quillen, A. C., & Faber, P. 2006, MNRAS, 373, 1245
Rebollido, I., Eiroa, C., Montesinos, B., et al. 2018, A&A, 614, A3
Rodrigo, C., & Solano, E. 2020, in Contributions to the XIV.0 Scientific Meeting (virtual) of the Spanish Astronomical Society, 182
Rodrigo, C., Solano, E., & Bayo, A. 2012, SVO Filter Profile Service Version 1.0, IVOA Working Draft 15 October 2012
Schmid, H. M., Joos, F., & Tschan, D. 2006, A&A, 452, 657
Schneider, G., Grady, C. A., Hines, D. C., et al. 2014, AJ, 148, 59
Sibthorpe, B., Kennedy, G. M., Wyatt, M. C., et al. 2018, MNRAS, 475, 3046
Singh, G., Bhowmik, T., Boccaletti, A., et al. 2021, A&A, 653, A79
Smirnov-Pinchukov, G. V., Moór, A., Semenov, D. A., et al. 2022, MNRAS, 510, 1148
Strubbe, L. E., & Chiang, E. I. 2006, ApJ, 648, 652
Takeuchi, T., & Artymowicz, P. 2001, ApJ, 557, 990
Thébault, P. 2009, A&A, 505, 1269
Thébault, P. 2012, A&A, 537, A65
Thébault, P., & Augereau, J. C. 2007, A&A, 472, 169
Thébault, P., & Kral, Q. 2018, A&A, 609, A98
Thébault, P., & Kral, Q. 2019, A&A, 626, A24
Thébault, P., & Wu, Y. 2008, A&A, 481, 713
Thébault, P., Kral, Q., & Ertel, S. 2012, A&A, 547, A92
Thébault, P., Kral, Q., & Augereau, J. C. 2014, A&A, 561, A16
van Holstein, R. G., Girard, J. H., de Boer, J., et al. 2020, A&A, 633, A64
van Holstein, R. G., Stolker, T., Jensen-Clem, R., et al. 2021, A&A, 647, A21
Wisdom, J. 1980, AJ, 85, 1122
Wright, E. L., Eisenhardt, P. R. M., Mainzer, A. K., et al. 2010, AJ, 140, 1868
Wyatt, M. C. 2005, A&A, 433, 1007
Wyatt, M. C., Smith, R., Su, K. Y. L., et al. 2007, ApJ, 663, 365
Yelverton, B., Kennedy, G. M., Su, K. Y. L., & Wyatt, M. C. 2019, MNRAS, 488, 3588
Zuckerman, B., & Song, I. 2012, ApJ, 758, 77

Appendix A: Stellar properties

We determined the stellar parameters by comparing the observed SED, corrected to the extinction, to the Kurucz models (Castelli & Kurucz 2003). We used a grid of stellar spectra with an effective temperature range between 8000 K and 9750 K, a sampling of 250 K, and a log g ranging between three and five, with a sampling of 0.5. For each Kurucz stellar spectrum, we computed the synthetic photometry for the ten filters used; their properties were obtained from the Spanish Virtual Observatory's (SVO) Filter Profile Service (Rodrigo et al. 2012; Rodrigo & Solano 2020). The filters used are TYCHO (B and G), Gaia DR2 (Gbp, G and Grp), 2MASS (J, H and Ks), and WISE ($W1$ and $W2$). The synthetic SED was fitted to the observed SED where the scaling factor corresponds to the dilution factor $(R_\star/d_\star)^2$, $d_\star$ is the known distance in parsec, and $R_\star$ is the stellar radius in units of solar radius. The best stellar spectrum was obtained by minimizing the goodness of fit for each spectrum of the grid. The stellar parameters of the best-fit solution are $T_\star = 9500$ K, $\log g = 5.0$, $R_\star = 1.54\,R_\odot$, and $L_\star = 17.64\,L_\odot$. We determined $R_\star$ using the dilution factor. From the stellar luminosity, we also derived the stellar mass from the mass-luminosity relation for main sequence star $L_\star = M_\star^{3.5}$, which gives $M_\star = 2.27\,M_\odot$. The best Kurucz stellar spectrum is shown in Fig. A.1 and used in the section 5 for the `MCFOST` analysis.

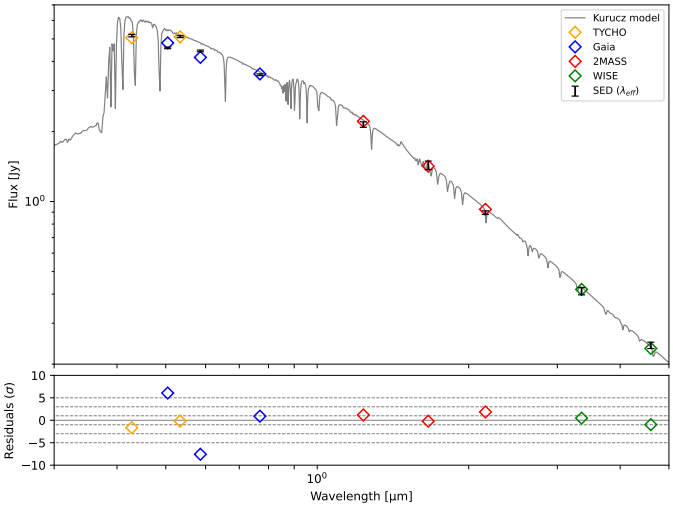

Fig. A.1. Kurucz stellar spectrum for a star with $T_{\rm eff} = 9500$ K and $\log g = 5.0$ (gray line). The synthetic SED computed with the Kuzucz model is indicated with colored diamonds, and the observational SED is shown with black dots. The lower panel shows the residuals between synthetic photometries and the SED in number of σ.

Appendix B: MCMC analysis of the `DDiT` model

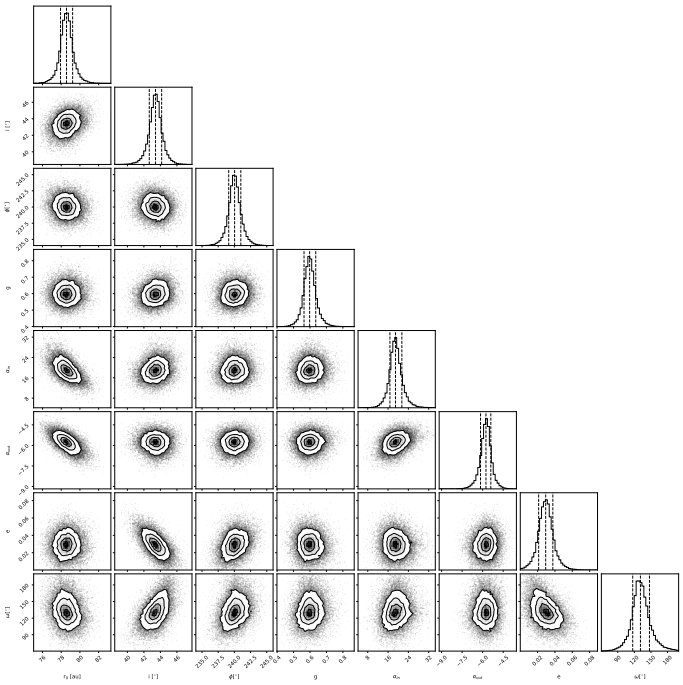

Fig. B.1. Corner plot for the MCMC analysis. From left to right and top to bottom: a (r_0), i, ϕ, g, $\alpha_{\rm in}$, $\alpha_{\rm out}$, e and ω. The interior vertical dashed lines are the more probable value, and the outer vertical dashed lines are the 1-σ error.